Application of TRMM PR and TMI Measurements to Assess Cloud Microphysical Schemes in the MM5 for a Winter Storm

MEI HAN

Goddard Earth Sciences and Technology Center, University of Maryland, Baltimore County, Baltimore, and Mesoscale Atmospheric Process Branch, Laboratory for Atmospheres, NASA Goddard Space Flight Center, Greenbelt, Maryland

SCOTT A. BRAUN

Mesoscale Atmospheric Process Branch, Laboratory for Atmospheres, NASA Goddard Space Flight Center, Greenbelt, Maryland

WILLIAM S. OLSON

Joint Center for Earth Systems Technology, University of Maryland, Baltimore County, Baltimore, and Mesoscale Atmospheric Process Branch, Laboratory for Atmospheres, NASA Goddard Space Flight Center, Greenbelt, Maryland

P. OLA G. PERSSON

Cooperative Institute for Research in Environmental Sciences, University of Colorado, and NOAA/Earth System Research Laboratory, Boulder, Colorado

JIAN-WEN BAO

NOAA/Earth System Research Laboratory, Boulder, Colorado

(Manuscript received 17 June 2009, in final form 8 January 2010)

ABSTRACT

This paper uses observations from Tropical Rainfall Measuring Mission (TRMM) precipitation radar (PR) and microwave imager (TMI) to evaluate the cloud microphysical schemes in the fifth-generation Pennsylvania State University–National Center for Atmospheric Research Mesoscale Model (MM5; version 3.7.4) for a wintertime frontal precipitation system over the eastern Pacific Ocean. By incorporating a forward radiative transfer model, the radar reflectivity and brightness temperatures are simulated and compared with the observations at PR and TMI frequencies. The main purpose of this study is to identify key differences among the five schemes [including Simple ice, Reisner1, Reisner2, Schultz, and Goddard Space Flight Center (GSFC) microphysics scheme] in the MM5 that may lead to significant departures of simulated precipitation properties from both active (PR) and passive (TMI) microwave observations. Radiative properties, including radar reflectivity, attenuation, and scattering in precipitation liquid and ice layers are investigated. In the rain layer, most schemes are capable of reproducing the observed radiative properties to a reasonable degree; the Reisner2 simulation, however, produces weaker reflectivity and stronger attenuation than the observations, which is possibly attributable to the larger intercept parameter (N_{0r}) applied in this run. In the precipitation ice layer, strong evidence regarding the differences in the microphysical and radiative properties between a narrow cold-frontal rainband (NCFR) and a wide cold-frontal rainband (WCFR) within this frontal precipitation system is found. The performances of these schemes vary significantly on simulating the microphysical and radiative properties of the frontal rainband. The GSFC scheme shows the least bias, while the Reisner1 scheme has the largest bias in the reflectivity comparison. It appears more challenging for the model to replicate the scattering signatures obtained by the passive sensor (TMI). Despite the common problem of excessive scattering in the WCFR (stratiform precipitation) region in every simulation, the magnitude of the scattering maximum seems better represented in the Reisner2 scheme. The different types of precipitation ice, snow, and graupel are found to behave differently in the relationship of scattering versus reflectivity. The determinative role of the precipitation ice particle size distribution (intercept parameters) is extensively discussed through sensitivity tests and a single-layer radiative transfer model.

Corresponding author address: Mei Han, Mesoscale Atmospheric Process Branch, Laboratory for Atmospheres, NASA/GSFC, Code 613.1, Greenbelt, MD 20771.
E-mail: mei.han@nasa.gov

DOI: 10.1175/2010JAMC2327.1

© 2010 American Meteorological Society

1. Introduction

With high spatial and temporal resolution, regional mesoscale models commonly have cloud-resolving capability; that is, they numerically represent the cloud and precipitation microphysical processes using various cloud microphysical schemes. This cloud-resolving capability enables mesoscale models to be widely used in weather and regional climate modeling, as well as providing a cloud and radiation database for use in satellite precipitation retrievals (Kummerow et al. 2001). There are a large number of microphysical schemes available in mesoscale models (e.g., Dudhia 1989; Tao and Simpson 1993; Reisner et al. 1998; Schultz 1995; Thompson et al. 2004). Model simulations, however, are very sensitive to the choice of microphysical scheme and the schemes are a large source of uncertainty in numerical weather prediction (Gilmore et al. 2004; McFarquhar et al. 2006), regional climate modeling (Liu and Moncrieff 2007), and satellite precipitation retrieval algorithms (Mugnai et al. 2008).

The fifth-generation Pennsylvania State University–National Center for Atmospheric Research Mesoscale Model (MM5; e.g., Anthes and Warner 1978) has undergone more than three decades of development. Along with its successor, the Weather Research and Forecasting (WRF) model, they are the most widely used mesoscale models. A majority of the different microphysical schemes available in these models are one-moment bulk microphysical parameterization schemes that originated from Kessler (1969) and Lin et al. (1983). These schemes only predict mixing ratios of various categories of water species (such as water vapor, cloud water, cloud ice, snow, graupel, and rain). Microphysical processes involving formation and growth of each water species (or in other words, partitioning of water among its various phases and hydrometeor types) are achieved through a basic assumption that the sizes of precipitation particles follow a certain statistical distribution. Following Marshall and Palmer (1948), the particle size distribution (PSD) of each precipitation species is often treated with an inverse exponential form,

$$N(D) = N_0 e^{-\lambda D}, \tag{1}$$

where N_0 is the intercept parameter, λ is the slope parameter, and $N(D)\ dD$ is the number of particles per unit volume with diameters between D and $D + dD$. Particularly, in the different schemes of the MM5, N_0 is either assigned a constant value or allowed to vary with the mixing ratios of water species or air temperature. After N_0 is determined, λ is calculated from the mixing ratio at each model grid point (e.g., Lin et al. 1983), using

$$\lambda = \left(\frac{\pi \rho N_0}{\rho_{\mathrm{air}} q}\right)^{0.25}, \tag{2}$$

where ρ and q are the density and mixing ratio, respectively, of each precipitation hydrometeor species, and ρ_{air} is the air density. In physical terms, these variables implicitly determine the size (e.g., the median volume diameter, $D_0 = 3.67/\lambda$; Kessler 1969, p. 27) of precipitation particles within one model grid point, which further controls terminal velocities, particle cross-sectional areas for collection, etc. Therefore, the differences in N_0 among these schemes may have a large impact on the performance of these microphysical schemes. Gilmore et al. (2004) indeed found a large sensitivity in the precipitation type and storm structures caused by the intercept parameter of graupel for a supercell storm.

Since precipitation particles directly interact with microwave radiation, the combination of satellite-borne active and passive microwave sensors provide a valuable platform for evaluating model microphysical schemes (Matsui et al. 2009; Li et al. 2009). In this paper, we use the observations from the National Aeronautics and Space Administration (NASA) and Japan Aerospace Exploration Agency (JAXA) Tropical Rainfall Measuring Mission (TRMM) precipitation radar (PR) and microwave imager (TMI) to evaluate the cloud microphysical schemes in the MM5, version 3.7.4 (this version was released in October 2006 and has since been frozen; more information is available at http://www.mmm.ucar.edu/mm5/mm5v3/v3mm5-chg-v3-7.html), for a wintertime frontal precipitation event. Instead of evaluating mesoscale simulations directly against the satellite retrieval products (e.g., rainfall, hydrometeor profiles), a radiative transfer model (Olson et al. 2001a,b) is used to convert the mesoscale model output to simulated radar reflectivities and microwave brightness temperatures for a direct comparison with the PR and TMI observations. The main purpose for using this method is to avoid inconsistencies in the physical assumptions (like thermodynamic environment and particle size distributions) between the mesoscale model and the retrieval algorithms, as well as inconsistencies between the TMI and PR retrieval algorithms themselves (Kummerow et al. 2001).

While the differences in the microphysical schemes in the MM5 are sometimes subtle and often complex, the purpose of this study is to identify key differences among these schemes that may lead to significant departures of simulated precipitation properties from both active (PR) and passive (TMI) microwave observations. The microphysical schemes in the mesoscale model, the experimental design, and the radiative transfer model are

introduced in section 2. Section 2 also establishes parameters for evaluating the column radiative properties of the precipitation hydrometeors. The TRMM PR and TMI observations are described in section 3. Model simulations based upon five different microphysical schemes and sensitivity tests for one of these schemes are included in section 4, emphasizing differences in the distributions of the liquid and solid precipitation hydrometeors and their radiative properties. In section 5, model evaluations are performed from a statistical perspective with a focus on comparisons to liquid and ice-phase precipitation signatures from one sensor (PR) or from both sensors (PR and TMI), respectively. Simulations and observations also suggest partitioning of the microwave radiative impacts of snow and graupel. In section 6, a single-layer model for precipitation ice is employed to elucidate the differences of the radiative properties of the precipitation hydrometeors in all of the simulations. This simplified model also provides an explanation for the differences seen in the distribution and radiative properties of snow and graupel associated with the simulated frontal precipitation system. The influence of the intercept parameter N_0 on each scheme's performance is extensively discussed.

2. Numerical model and radiative parameters

a. Mesoscale model and experiment design

There are five ice microphysics schemes available in the MM5 V3.7.4. These schemes are known as, simple ice (Dudhia 1989), Reisner1 mixed phase (Reisner et al. 1998), Reisner2 graupel (Reisner et al. 1998; Thompson et al. 2004), Schultz (Schultz 1995), and Goddard (Tao and Simpson 1993).

Dudhia's simple ice scheme (hereinafter labeled Simple) is modified from a warm rain scheme. It includes only two prognostic variables of hydrometeors that represent cloud liquid water (or cloud ice) and rain (or snow), depending on whether the temperature is above (or below) 0°C. The scheme does not allow supercooled water. Ice and snow immediately melt when the temperature is warmer than 0°C, and cloud water and rain freeze when the temperature is colder than 0°C.

The Reisner1 mixed-phase scheme (hereinafter Reisner1) contains four prognostic variables that explicitly predict the mixing ratios of four categories of hydrometeors: cloud liquid water, rain, cloud ice, and snow. It thus allows the simultaneous presence of liquid and ice water substance. More description can be found in Reisner et al. (1998). The intercept parameter for the snow size distribution, N_{0s}, is defined as a function of the snow mixing ratio (q_s):

$$N_{0s} = \left\{1.718\left[\frac{1}{\rho_{\mathrm{air}} q_s \alpha}\left(\frac{\pi \rho_s}{\rho_{\mathrm{air}} q_s}\right)^{b_s/4}\right]^{0.94}\right\}^{4/(4-0.94 b_s)}, \quad (3)$$

where $1/\alpha = 6\rho_w/a_s\Gamma(4 + b_s)$, $a_s = 11.72$, $b_s = 0.41$, ρ_s (=100 kg m^{-3}) is the snow particle density, and ρ_w (=1000 kg m^{-3}) is the liquid water density. As q_s decreases, N_{0s} increases until reaching the specified upper bound (2×10^7 m^{-4}).

The Reisner2 graupel scheme (hereinafter Reisner2) includes five categories of hydrometeors. In addition to the four types of hydrometeors as in Reisner1, it includes graupel as a fifth hydrometeor. It also explicitly predicts the number concentration of cloud ice (Reisner et al. 1998). Thompson et al. (2004) improved the original Reisner2 scheme in many respects, including a modified N_{0s} that is temperature (T) dependent as opposed to a mixing ratio dependent intercept as in Reisner1. It follows the relationship

$$N_{0s} = \min\{2 \times 10^8, 2 \times 10^6 \times \exp[-0.12 \min(-0.001, T - T_0)]\}, \quad (4)$$

where $T_0 = 273.15$ K. The intercept parameter for graupel (N_{0g}) is a function of the graupel mixing ratio (q_g):

$$N_{0g} = 2.38 \times \left(\frac{\pi \rho_g}{\rho_{\mathrm{air}} q_g}\right)^{0.92}, \quad (5)$$

where ρ_g (=400 kg m^{-3}) is the graupel particle density. As q_g decreases, N_{0g} increases until reaching the specified upper bound (4×10^6 m^{-4}). The intercept parameter for rain (N_{0r}) is a function of the rain mixing ratio (q_r):

$$N_{0r} = 0.5 \times (N_{0r_max} - N_{0r_min}) \times \tanh\left(\frac{q_{rc} - q_r}{0.5 \times q_{rc}}\right) + 0.5 \times (N_{0r_max} + N_{0r_min}), \quad (6)$$

where $N_{0r_max} = 1 \times 10^9$ m^{-4}, $N_{0r_min} = 2 \times 10^7$ m^{-4}, and $q_{rc} = 0.0002$ g kg^{-1}.

The Schultz microphysics scheme (hereinafter Schultz) is a five-class hydrometeor scheme designed for high computational efficiency for operational weather forecasting. Unlike the other bulk schemes in the MM5, this scheme does not make explicit assumptions concerning the intercept parameters of the PSD. Instead, conversion rates are often expressed in terms of a tunable parameter whose value is set to match conversion rates described in a wide array of studies. Since some assumption about the PSD is required for the radiative transfer calculations, the inverse exponential form is assumed for

TABLE 1. Precipitation hydrometeor intercept parameters in seven simulations. Note: Schultz scheme does not explicitly specify hydrometeors' intercept values. For this scheme, the quantities listed are based on standard values.

Simulations		MM5 V3.7.4 default code					Sensitivity tests for GSFC scheme	
		Simple	Reisner1	Reisner2	Schultz	GSFC	GSFC_ds	GSFC_dg
Intercepts (m^{-4})	Snow	$N_{0s} = 2.0 \times 10^7$	$1.2 \times 10^5 \leq N_{0s}(Q_s) \leq 2.0 \times 10^7$	$2.0 \times 10^6 \leq N_{0s}(T) \leq 2.0 \times 10^8$	$N_{0s} = 3.0 \times 10^6$	$N_{0s} = 1.0 \times 10^8$	$N_{0s} = 4.0 \times 10^6$	Same as GSFC
	Graupel	—	—	$3.3 \times 10^5 \leq N_{0g}(Q_g) \leq 4.0 \times 10^6$	$N_{0g} = 4.0 \times 10^6$	$N_{0g} = 4.0 \times 10^6$	Same as GSFC	$N_{0g} = 4.0 \times 10^5$
	Rain	$N_{0r} = 8.0 \times 10^6$	$N_{0r} = 8.0 \times 10^6$	$2.0 \times 10^7 \leq N_{0r}(Q_r) \leq 1.0 \times 10^9$	$N_{0r} = 8.0 \times 10^6$	$N_{0r} = 8.0 \times 10^6$	Same as GSFC	Same as GSFC

the Schultz scheme. The N_{0r} and N_{0s} follow those in Lin et al. (1983), while N_{0g} follows Rutledge and Hobbs (1984). See Table 1 for their values.

The Goddard microphysics scheme (GSFC) is also a five-class hydrometeor scheme that includes the same cloud and precipitation species as in Reisner2 and Schultz. It is primarily based on Lin et al. (1983) with the inclusion of graupel (Rutledge and Hobbs 1984; McCumber et al. 1991). GSFC has undergone some important improvements; for example, the implementation of a saturation adjustment scheme (Tao et al. 1989) and modifications related to graupel PSD, density, fall speed, cloud ice nucleation, and depositional growth (Braun and Tao 2000).

To evaluate the performance of each microphysics scheme in the MM5 for a case of wintertime cold-frontal rainbands, seven simulations[1] were conducted. Five simulations were carried out using the default code (MM5 V3.7.4) of each scheme described previously. In addition, two simulations using the GSFC scheme, but with decreased intercept parameters for snow and graupel were performed. The two additional simulations are named GSFC_ds and GSFC_dg, respectively. While there are many differences among the various microphysics schemes, the purpose of this study is to identify the major differences in comparisons with observations from both PR and TMI. Therefore, we list one of the notable differences among these simulations; that is, the intercept parameter, N_0, for each precipitation hydrometeor species in Table 1. The Simple and GSFC runs use fixed N_0 values for rain, snow, and graupel. The Reisner1 and -2 runs use variable N_0 values calculated with Eqs. (3)–(6), with the ranges of the N_0 values listed in Table 1. Overall, N_0 varies about three orders of magnitudes (from 10^5 to 10^8 m^{-4}) for snow and one order of magnitude (from 10^5 to 10^6 m^{-4}) for graupel using the default code. The N_0 values in the two sensitivity tests of the GSFC scheme are also within this range of variation. For rain, each scheme uses 8×10^6 m^{-4} from the original Marshall–Palmer raindrop size distribution (Marshall and Palmer 1948), with the exception of Reisner2, which uses a larger value (varying from 10^7 to 10^9 m^{-4}). Note that the N_0 values shown in Table 1 for the Schultz scheme are not actually used in the Schultz scheme, but instead are assumed for the purpose of running the radiative transfer models. The density of snow (ρ_s = 100 kg m^{-3}) and graupel (ρ_g = 400 kg m^{-3}) are the same in each simulation.

b. *Radiative transfer calculations and parameters in use*

To examine the capability of the different microphysics schemes in replicating the precipitation properties observed by the TRMM PR and TMI, the model output fields from the seven MM5 simulations (5-km horizontal spacing) are incorporated into a radiative transfer model (Olson et al. 2001a,b) to calculate the radar reflectivities and upwelling brightness temperatures at the PR and TMI frequencies. The calculations use the same PSDs (N_0 values) for each scheme (except Schultz) as used in the mesoscale model. Since there are no specified N_0 values in the Schultz scheme, evaluation of the radiative transfer calculations is not as straightforward as for other schemes. However, by assuming standard values of N_0 for the Schultz run (see Table 1), the simulated radiative properties can still provide an estimate to be compared with the TRMM microwave measurements. The representativeness of such assumptions will be noted in later analyses.

Mie theory is used for estimating the backscattering cross section in the reflectivity calculations. This method is in contrast to the general usage in many previous studies (e.g., Fovell and Ogura 1988; Braun 2006; McFarquhar et al. 2006; Han et al. 2009) of the Rayleigh approximation, which simply relates the backscattering cross section to the sixth moment of the particle size. The Rayleigh

[1] The model configurations, other than the microphysical schemes, are identical to a previous paper for the same case (Han et al. 2009).

approximation is applicable when the particle size parameter $\alpha \ll 1$ ($\alpha = 2\pi a/\lambda$, where a is the radius of a precipitation particle and λ is the wavelength of radiation; Battan 1973, pp. 36–38). When compared with observations taken by radars with relatively low frequencies [e.g., the S-band Weather Surveillance Radar-1988 Doppler (WSR-88D)], the model simulation of radar reflectivity based on the Rayleigh approximation should be accurate. However, PR is a K_u-band radar operating at 13.8 GHz. At this frequency, the Rayleigh approximation is not strictly valid if sufficient numbers of large precipitation particles are present.

The upwelling brightness temperatures are calculated at two frequencies, 19 and 85 GHz, consistent with the TMI channels operating at these frequencies. At 19 GHz, the brightness temperature is mainly sensitive to emission due to the rain layer below the freezing level. At 85 GHz, TMI detects the brightness temperature depression (i.e., the reduction of radiance as compared to the background) due to scattering by precipitation ice.[2] However, because there is a considerable amount of ambiguity in directly interpreting the raw brightness temperatures in terms of precipitation properties (Petty 1994), this study uses two parameters that are quasilinear transformations of the single-frequency, dual-polarization brightness temperatures introduced by Petty and Katsaros (1990) and Petty (1994). They are the attenuation index (P) and scattering index (S). The attenuation index is also called the normalized polarization (therefore symbolized by P) and is formulated as

$$P = \frac{T_V - T_H}{T_{V,0} - T_{H,0}}, \tag{7}$$

where T_V and T_H are the observed or simulated vertically and horizontally polarized brightness temperatures at a given frequency, and $T_{V,0}$ and $T_{H,0}$ are the corresponding brightness temperatures for the same scene in the absence of all cloud and precipitation (also called clear-air pixels). Normalized polarization P decreases as the attenuation due to precipitation increases, with its value varying approximately between 0 and 1 (0 corresponds to a completely opaque rain cloud; 1 corresponds to a cloud-free ocean scene). The scattering index (K) is

$$S = PT_{V,0} + (1 - P)T_c - T_V, \tag{8}$$

where P is the normalized polarization, and T_c represents the brightness temperature of a hypothetical, optically thick, and nonscattering cloud–rain layer. Here, it is assumed that $T_c = 273$ K to represent the layer bounded by the freezing level. Scattering index S increases with increasing scattering by precipitation ice.

In this study, the attenuation index at 19 GHz (P19) and the scattering index at 85 GHz (S85) are derived from TMI brightness temperatures, as well as model-simulated brightness temperatures. For the observational indices, the clear-air pixel value is estimated from selected cloud-free points at approximately 100–300 km away from (behind and ahead of) the precipitation band. Given the potentially large contrast in the water vapor field behind and ahead of the cold front, an average is taken among these points with an attempt to minimize the influence of the water vapor contrast in the calculation of P. In the model simulation, the clear-air pixel value is calculated with all the cloud and precipitation hydrometeors removed from the atmosphere. Since the 19- and 85-GHz channels are mainly sensitive to the column-integrated rain and precipitation ice, respectively, the two parameters, P19 and S85, generally represent the attenuation (or transmittance) from the rain layer and the scattering from the precipitation ice layer, respectively.

In an attempt to derive radar quantities that represent the ''columnar'' sensitivities of P19 and *S85*, both observed and simulated reflectivities are averaged[3] within the rain and precipitation ice layers, respectively. In winter frontal precipitation systems, freezing levels vary significantly from the warm sector to the cold sector. In the PR observations for this case, a layer of enhanced reflectivity indicates a melting layer at approximately 1.5–2.0 km MSL on the warm side and at approximately 1.0–1.5 km MSL on the cold side of the rainband. The simulations suggest similar variations. Therefore, we define a rain-layer mean reflectivity as the average from 0 to 1.5 km MSL, and a precipitation ice-layer mean reflectivity as the average from 2.5 to 5 km MSL for the PR observations. In the simulations, since the freezing level is known, the layer mean reflectivity for rain is defined as the average in the layer between the ocean surface and the model level immediately below 0°C. The layer mean reflectivity for precipitation ice is the average from the model level immediately above 0°C to 5 km. It should be noted that the rain layer, as defined above, includes a sublayer that involving melting processes, where ice particles are coated with liquid water that influence dielectric properties of the particles. This microphysical characteristic of melting ice is very important in both active and passive radiative transfer calculations (Olson

[2] Since TMI cannot clearly differentiate the scattering due to snow or graupel, the term ''precipitation ice'' is frequently used when no intention of partitioning their individual contributions is made.

[3] The average is performed for reflectivity in linear units ($mm^6\ m^{-3}$).

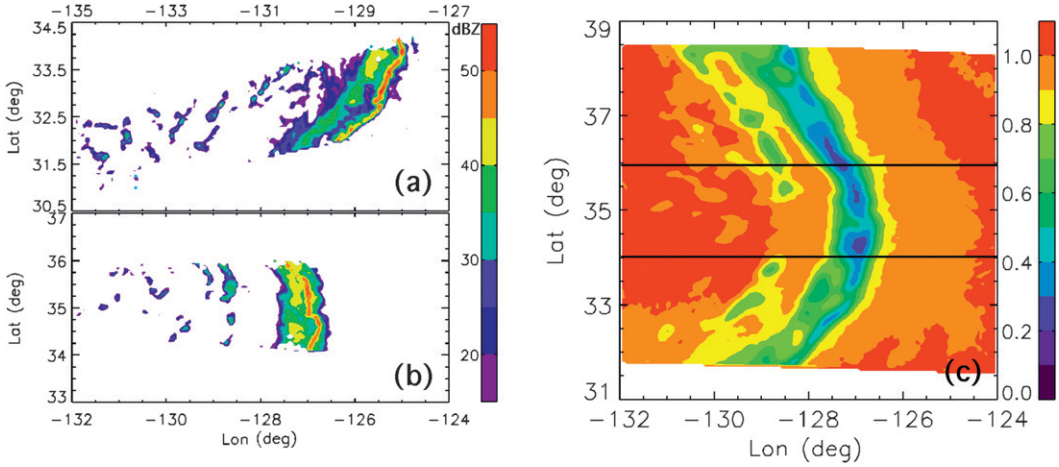

FIG. 1. The PR layer mean (0–1.5 km) radar reflectivity (dBZ) for rain at (a) 0023 and (b) 0200 UTC 19 Feb 2001. (c) TMI attenuation index at 19 GHz (P19) at the same time as in (b). PR has a narrower swath (215 km) than that of TMI (759 km). Black lines in (c) outline the PR swath in (b).

et al. 2001a,b). However, the current bulk microphysics schemes in mesoscale models do not have this degree of sophistication and the radiative consequence of melting therefore is not included in the current study.

3. TRMM PR and TMI observations

The TRMM PR and TMI observed an intense cold-frontal precipitation system during three consecutive overpasses at approximately 0023, 0200, and 0337 UTC 19 February 2001. Han et al. (2009) analyzed variability of the structure of the precipitation system using TRMM observations (see their Fig. 2) and an MM5 simulation. In this paper, analysis is focused on the first two overpasses (0023 and 0200 UTC) because the third overpass (0337 UTC) only has limited coverage of the southern end of the frontal rainband.

Figure 1 shows the PR layer mean reflectivity in the rain layer and the attenuation index at 19 GHz (P19). With high horizontal resolution (4.3 km), the PR layer mean reflectivity (Figs. 1a,b) clearly delineates the frontal rainband and the postfrontal rain showers. The frontal rainband consists of an intense narrow cold-frontal rainband (NCFR), with reflectivity up to 55 dBZ, and a wide cold-frontal rainband (WCFR), with somewhat weaker reflectivity.[4] The NCFR was located at the leading edge of/or embedded within the WCFR. In Fig. 1c, P19 shows a bowed band of attenuation associated with the frontal rainband. Because the TMI 19-GHz channel has a horizontal resolution of 18 × 30 km in its elliptical footprint, P19 could not generally differentiate the attenuation because of the NCFR and the WCFR. However, it clearly shows that the attenuation is greater (with smaller P19 values) in areas of more intense rainfall.

Figure 2 shows the PR layer mean reflectivity for precipitation ice and the scattering index at 85 GHz (S85). The radar-derived ice structure of the NCFR and WCFR (Figs. 2a,b) are similar to lower levels as seen from the radar-derived rain structure, but with the reflectivities decreased to ~40 dBZ for NCFR and to <30 dBZ for WCFR. The TMI 85-GHz channel has a high horizontal resolution of 5 km × 7 km and was able to detect smaller-scale scattering signatures (comparable to the structure observed by PR) related to precipitation ice. The ice in the NCFR contributes to the strongest scattering (up to ~86 K). Moving away from the NCFR, scattering due to the ice in the WCFR gradually decreases.

4. Model results

Model simulations at different times, nearly concurrent with the three TRMM satellite overpasses, have been examined in this study and a previous study for the same case (Han et al. 2009). It is shown that the simulations generally captured well the evolution of the rainband. The structure and intensity of the rainband was also generally steady during the 3–4-h period during which it was sampled by the satellite sensors. In this paper, model results at 0200 UTC, concurrent with the second TRMM overpass, are presented for the sake of brevity.

[4] The NCFR (~10 km wide) is typically observed along the sharp temperature gradient associated with an intense surface cold front. The WCFR (~100 km wide) is associated with an upper-level cold front that often marks the leading edge of a stratospheric PV intrusion (e.g., Han et al. 2009). If determined only based on their reflectivity and updraft intensities, the NCFR and WCFR could be classified loosely as convective and stratiform precipitation, respectively.

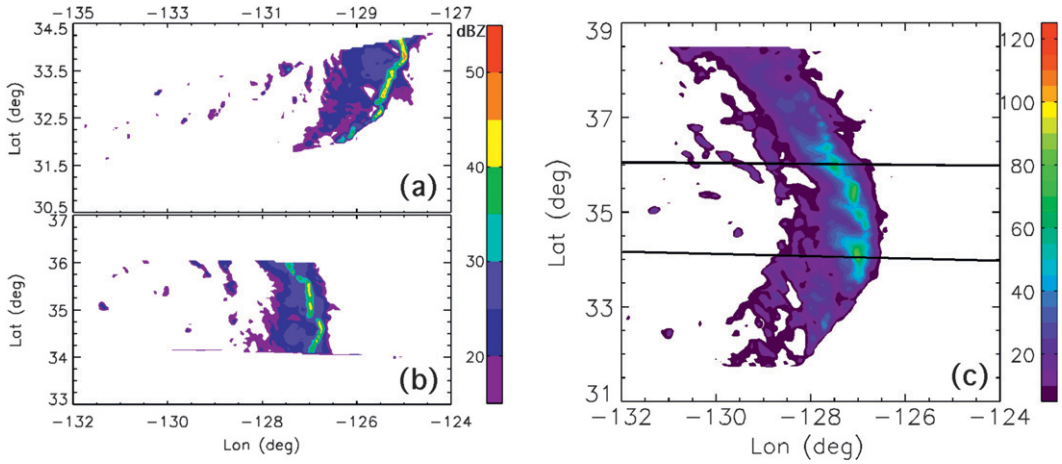

FIG. 2. As in Fig. 1, but for precipitation ice at (a) 0023 and (b) 0200 UTC 19 Feb 2001. (c) TMI scattering index at 85 GHz (S85) at the same time as in (b).

a. Reflectivities in rain and precipitation ice layers

The simulated reflectivity within the rain layer is shown in Fig. 3. All seven simulations captured the general morphology of the rainbands seen in the TRMM PR data; that is, the NCFR (high reflectivity) leading or embedded within the WCFR (moderate reflectivity). Reisner2 shows a relatively weak WCFR, while Schultz obtains much more intense reflectivities in the NCFR than other schemes and also produces a somewhat narrower WCFR.[5] Nevertheless, these simulations have replicated, to a reasonable degree, the structure of the observed rainband in the layer below the freezing level.

The simulated layer mean reflectivities for precipitation ice (Fig. 4) have a generally larger model-dependent variability in the precipitation structures than that seen within the rain layer. The Schultz run has the narrowest band of precipitation ice relative to the other runs. In most simulations, the NCFR and WCFR can be readily differentiated from their contrasts in reflectivity intensity. The simulated intensities of the NCFR are generally in agreement with, or slightly weaker than, the observations. However, the intensities of the WCFR are 5 to 10 dBZ higher in the Simple, Reisner1, Reisner2, Schultz, and GSFC_ds runs than the PR observations (see Figs. 2a,b). The GSFC and GSFC_dg runs produce a better agreement with the observations for the WCFR intensity.

[5] The narrowness of the band analyzed here and later in this study for the Schultz scheme is independent to the particle size distribution. However, the assumed N_0 values may have an impact on the intensity of the reflectivity that will be noted in later sections.

b. Vertical profiles of hydrometeors

To further compare the simulations, the mean vertical profiles of cloud and precipitation hydrometeors are shown in Fig. 5. These profiles are computed by averaging hydrometeor-mixing ratios within the area of interest (enclosed by the boxes shown in Figs. 3 and 4). Since the TMI and PR are not sensitive to cloud ice particles, the comparison of cloud ice amount in these simulations is not discussed in this study. It should be noted that these hydrometeor profiles at other times, during periods of similar frontal intensity, have been also examined and confirm that the analysis at 0200 UTC (Fig. 5) represents rather general characteristics of these schemes.

Considering the column-integrated water content, Fig. 5 shows that the Simple ice scheme produces the greatest precipitation content, while the Schultz scheme produces the least. For cloud liquid water, the Reisner1 and Reisner2 runs generate a deep layer of supercooled water extending up to 6 km. The supercooled cloud liquid water content is relatively small in the GSFC scheme, but it increases in the sensitivity run (GSFC_ds), where N_{0s} decreases by approximately two orders of magnitude. For rain, most of the simulations give an average mixing ratio of ~0.1 g kg^{-1} within the layer 1–2 km above the surface, except for Reisner2 which produces about 30%–40% more rain than the other schemes.

The profiles of precipitation ice (snow and graupel) vary dramatically from one scheme to another. The Simple ice scheme produces a very large amount of snow. Reisner1 also produces somewhat more snow than the other schemes. It may be attributed, to a certain degree, to the fact that snow is the only solid precipitation hydrometeor in these schemes. The amounts of snow and graupel in the Reisner2 and GSFC schemes are generally

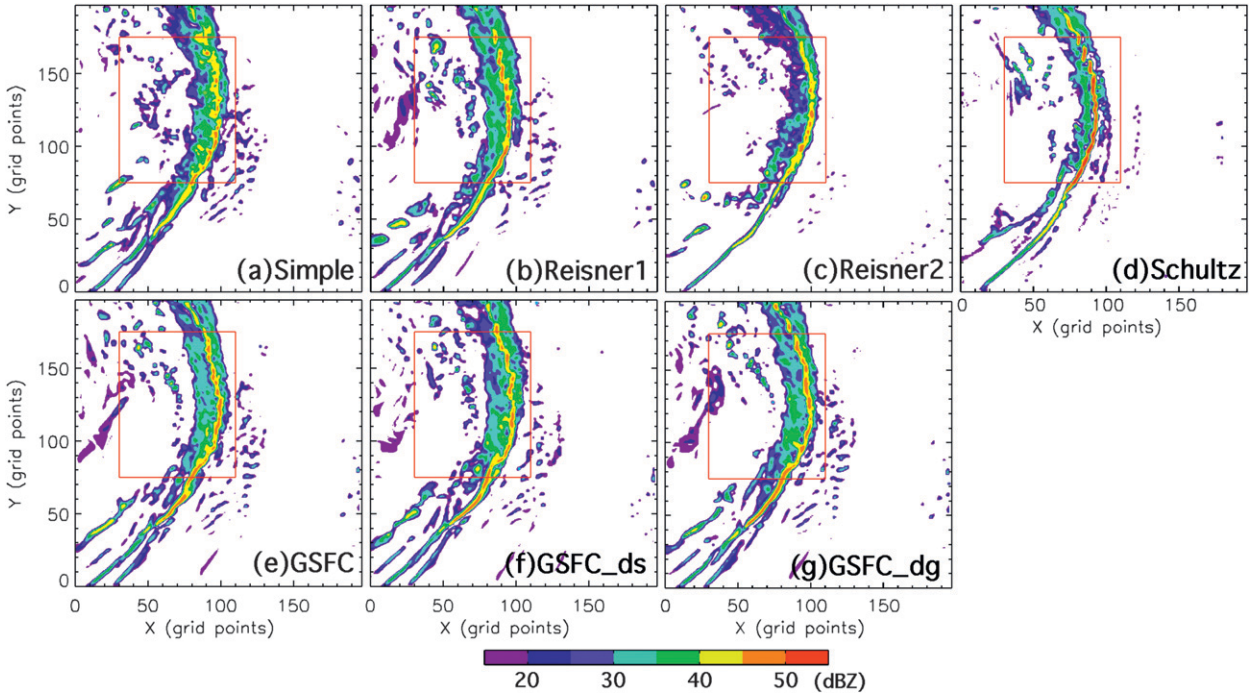

FIG. 3. MM5 layer mean reflectivity (dBZ) for rain at 0200 UTC 19 Feb 2001 for seven simulations. (a)–(e) Five different schemes, respectively. The sensitivity runs for the GSFC scheme with (f) decreased N_{0s} and (g) decreased N_{0g}. The red boxes outline the area with comparable scenes as seen by TRMM, which will be used in the later analyses of hydrometeor vertical profiles and statistical comparison.

comparable. As N_{0s} decreases ~2 order of magnitude in the GSFC_ds run, the snow amount decreases while other hydrometeors amounts increase, especially graupel. As N_{0g} decreases one order of magnitude in the GSFC_dg run, the graupel amount decreases while only the snow amount increases.

Although it is beyond the scope of this study to examine the mass budgets for each water species and to interpret the very detailed causes leading to the differences in the simulations using different microphysical schemes, the changes from the GSFC control run to the two sensitivity runs are briefly discussed here to set some background for later comparisons on radiative properties. In the GSFC_ds run, as the N_{0s} value is decreased, the snow particle sizes increase for a given mixing ratio at a given grid point, which contributes to larger terminal velocities and greater fallout of snow. The total snow amount consequently decreases (Fig. 5f). Accompanying these microphysical changes, updrafts in this area intensify compared to the control run (not shown), which leads to more supercooled cloud water and graupel. In the GSFC_dg run, the decreased N_{0g} contributes to larger graupel particles, which increases the terminal velocities, leads to greater graupel fallout, and ultimately to decreased graupel (Fig. 5g). With less collection of snow by graupel, snow amount increases.

c. *Simulated P19 and S85*

Figure 6 shows the horizontal distribution of the simulated attenuation index at 19 GHz P19 for GSFC run. The arch-shaped region of attenuation associated with the frontal rainband in the simulation is quite similar to the observations (see Fig. 1c). It is also consistent with the structure of the rain layer reflectivity (see Fig. 3e); that is, the strong reflectivity is associated with more intense attenuation. Other schemes and sensitivity runs show generally similar structures as seen in GSFC, with some differences in the width of the band that have been shown in the reflectivity field in Fig. 3 or subtle differences in their intensities that will be analyzed in a later comparison from a statistical perspective. The other P19 plots are not presented here in the interest of brevity.

The simulated scattering index at 85 GHz S85 is shown in Fig. 7. The overall magnitudes of the scattering for the Simple and GSFC runs are quite strong with notable portions of the scene having S85 greater than 80 K. The Reisner1, Reisner2, and Schultz runs have somewhat weaker scattering signatures and the scattering maxima in the Reisner2 run appears to be closer to the observed maximum magnitude (see Fig. 2c). However, whether the overall scattering is strong or weak, most of the runs produce maxima of scattering in both the narrow and

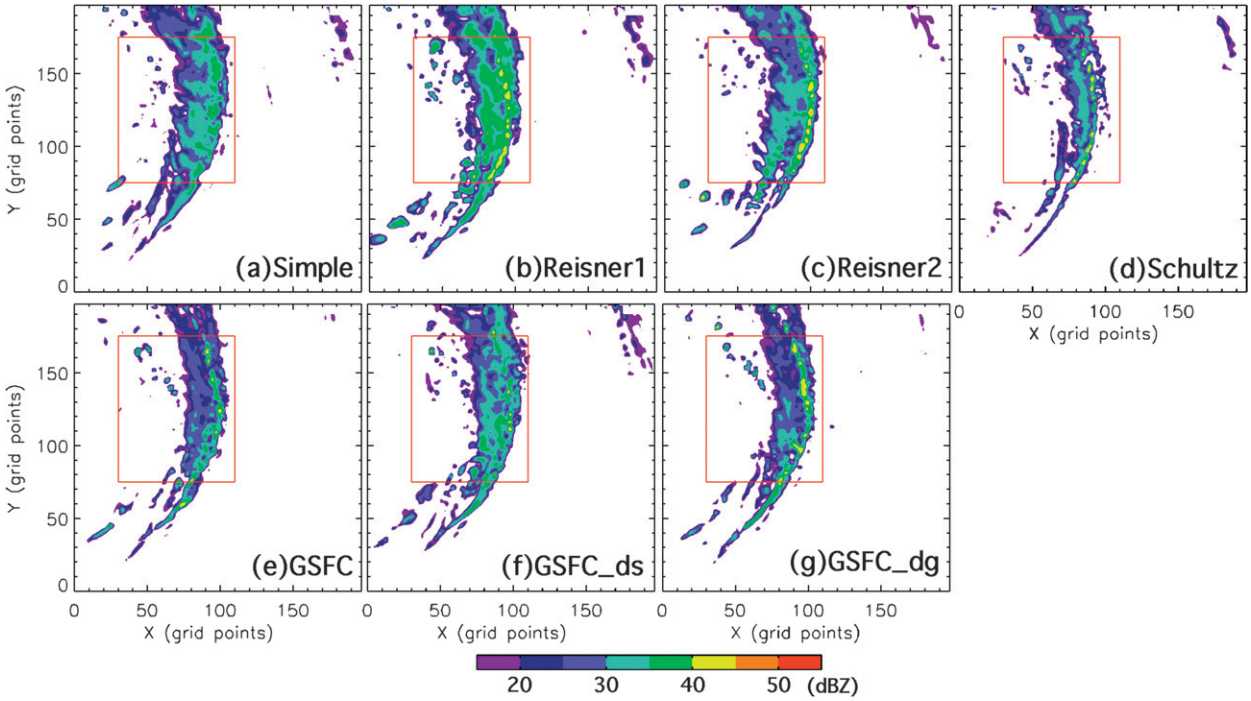

FIG. 4. As in Fig. 3, but for precipitation ice.

wide rainbands. This feature is different from the single scattering maximum associated with the NCFR seen in the observations. The Schultz run is an exception, with only one maximum of scattering within the frontal band; however, this maximum is collocated with the WCFR, rather than the NCFR as observed.

5. Statistical comparison between observations and model results

In this section, the parameters discussed in the previous sections are compared from a statistical perspective. Analysis is applied to the area of interest (enclosed by the boxes shown in Figs. 3, 4, 6, 7) in the model simulation at 0200 UTC, wherein the structure at this time is consistent with the PR and TMI observations in the overpasses at 0023 and 0200 UTC. First, the radar reflectivity from PR is compared to the simulated reflectivity using a histogram by altitude diagram, which is similar to the contoured frequency by altitude diagram (CFAD; Yuter and Houze 1995) except that the number of counts for each bin are not normalized by the total number of TRMM pixels at each level. Second, to evaluate the simulations against both TMI and PR observations, the attenuation index for rain (or scattering index for precipitation ice) is plotted as a function of the layer mean reflectivity. Further analysis of the partitioning of snow and graupel is also discussed.

a. *Radar reflectivity histograms by altitude*

The observed and simulated radar reflectivity histograms by altitude are shown in Fig. 8. The high-frequency areas in the diagrams mostly correspond to the WCFR, since the area occupied by the WCFR is much larger compared to that occupied by the NCFR. For example, in Fig. 8a, the observed frequency maximum is associated with reflectivities <30 dBZ in the precipitation ice layer, which corresponds to the magnitudes of reflectivities in the WCFR (see Figs. 2a,b).

When compared with the PR observations, the seven simulations (Figs. 8b–h) are generally seen to produce stronger reflectivities, especially in the WCFR. The Reisner1 run (Fig. 8c) produces a particularly large offset (~10 dBZ higher) of the frequency maximum relative to the observations in the precipitation ice layer. The Reisner1 ice-layer reflectivity also appears unreasonably strong relative to that of the corresponding rain layer. It may be inferred that the size of the snow particles (the only solid hydrometeors) in the Reisner1 simulation are likely too large and therefore produce excessive backscattering. This concern will be further addressed in section 6b. Considering all of the simulations, the frequency maximum in the reflectivity histograms from the Schultz, GSFC, and GSFC_dg runs show the best agreement with the observations with a high bias of 5 dBZ in Schultz and 2−3 dBZ in the GSFC and GSFC_dg runs. The GSFC_ds simulated reflectivity histogram does not

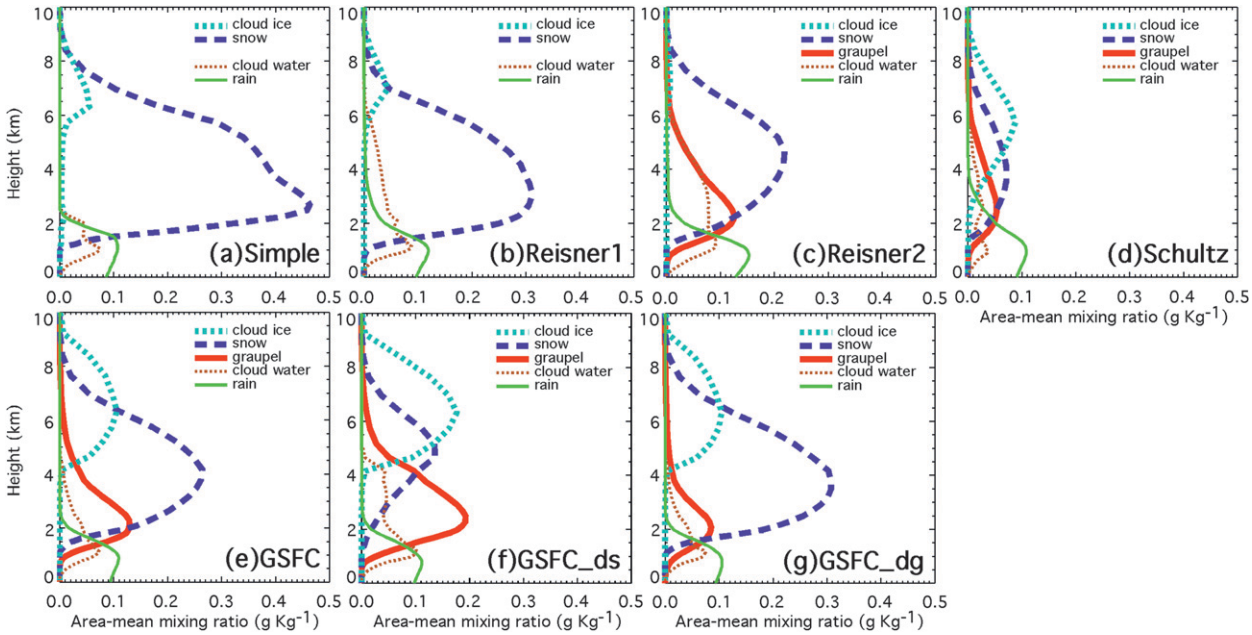

FIG. 5. MM5 mean vertical profiles of cloud and precipitation hydrometeors mixing ratio (g kg^{-1}) for seven simulations. The average is computed within the area enclosed by the box shown in Figs. 3 and 4.

agree with the observations as well as the control GSFC run likely because of the increase in graupel mass and possibly the increase in the mean diameter of the snow particles. The reflectivity histogram analysis is consistent with the earlier comparison of the layer mean reflectivities (see Figs. 2 and 4).

b. *P19 versus rain-layer mean reflectivity*

Comparison with radar reflectivity alone is inadequate since an increase (decrease) of N_0 typically leads to increases (decreases) in particle mixing ratio, but decreases (increases) in particle mean diameter and reflectance. A better approach is to combine information from the radar and radiometer since the former is sensitive to both particle size and mass content while the latter is mainly sensitive to mass content.

To make an evaluation using observations from both PR and TMI, the rain-layer mean reflectivity and the attenuation index at 19-GHz channel are incorporated into a 2D histogram. Because the TMI 19-GHz channel has a larger footprint than PR, the PR-observed layer mean reflectivity for rain is smoothed[6] to assure consistency with the TMI resolution. A similar smoothing technique was also applied to the simulated radar reflectivity since its horizontal resolution is much finer than that of the simulated TMI brightness temperatures.

Figure 9a shows P19 versus rain-layer mean reflectivity for the TRMM observations. The P19 values decrease (i.e., rain attenuation increases) with the increase in reflectivity. Results from the seven simulations (Figs. 9b–h) generally agree with the observed trend, with the most notable departures exhibited by the Reisner2 and

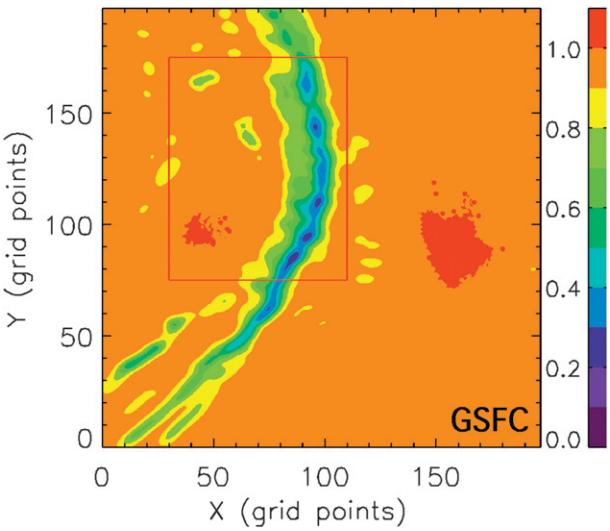

FIG. 6. MM5 attenuation index at 19 GHz (P19) for the GSFC run.

[6] A Gaussian kernel with half-power width of ~24 km (the average of the long and short axis of the elliptic footprint at the 19-GHz channel) is applied to PR and simulated reflectivities.

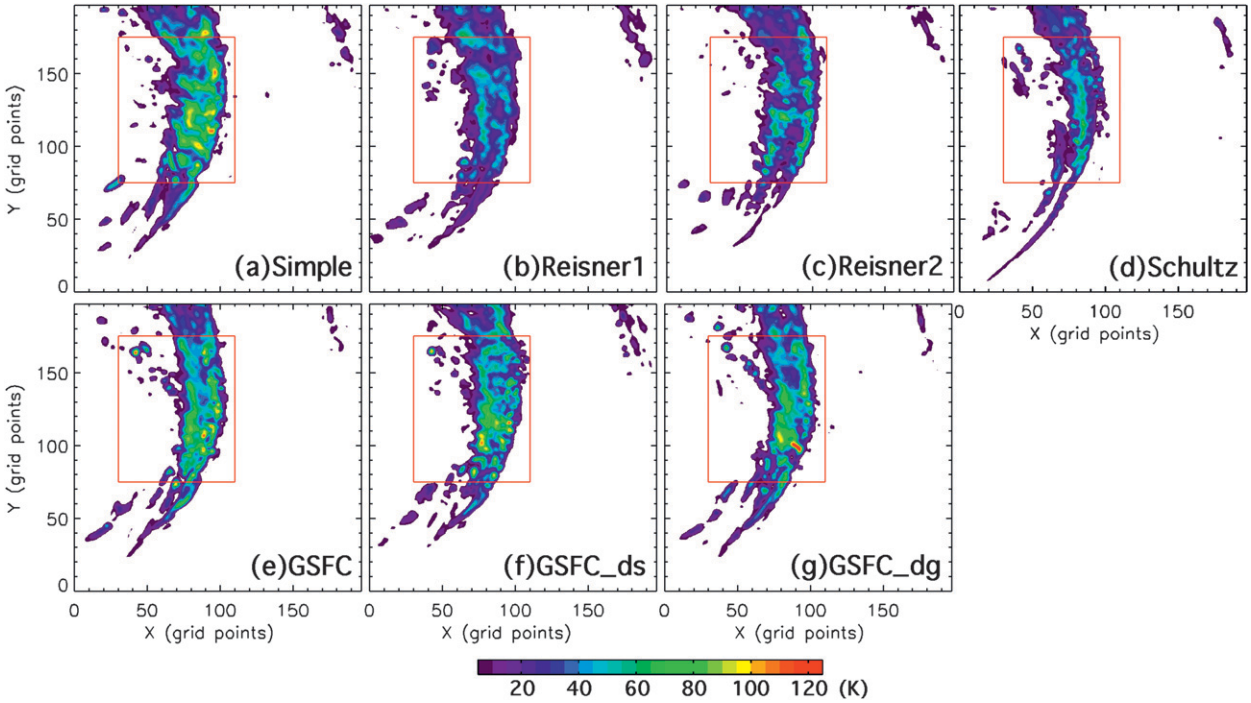

FIG. 7. MM5 scattering index at 85 GHz (S85) for seven simulations.

Schultz runs. In particular, the P19 values in Reisner2 (Fig. 9d) are typically ~0.1 units less than the PR observations for a given reflectivity. This feature is likely related to the larger amount of rain shown in the Reisner2 hydrometeor profile (see Fig. 5c), since attenuation is mainly sensitive to the column-integrated rain mass at 19 GHz. In addition, the Reisner2 run produces large amounts of cloud liquid water, which may slightly enhance the attenuation as well. Viewed another way, the reflectivity in Reisner2 is ~3 dBZ less (also see Fig. 3c) than the observations for a given P19 value. The smaller reflectivity suggests a smaller mean drop diameter for rain produced in this simulation. Equation (6) and Table 1 show that N_{0r} can vary from 2×10^7 to 1×10^9 m^{-4} in the Reisner2 scheme. Therefore, N_{0r} in Reisner2 is appreciably larger than the Marshall–Palmer (M–P) value of 8×10^6 m^{-4} that is used in other schemes. The larger N_{0r} value would contribute to smaller raindrops, lower reflectivities, as well as a greater mass of rain. For the Schultz run (Fig. 9e), the 2D histogram shows a positive bias of ~3 dBZ in simulated reflectivity for a given P19 relative to the PR values when the reflectivity is greater than 35 dBZ (consistent with the intense reflectivities seen in Fig. 3d). However, since the N_{0r} value is not explicitly specified in the Schultz scheme, the high bias suggests that the assumed N_{0r} value (taken from the M–P distribution) may not be the appropriate. The other cases agree well with the observed attenuation and reflectivity relationship; however, the spread in the 2D histograms are much narrower than observed.

c. *S85 versus precipitation ice-layer mean reflectivity*

To evaluate the performance of the ice-phase parameterizations, the 2D histograms of scattering index, *S85*, versus layer mean reflectivity are shown in Fig. 10 (note: the overlaid lines of red crosses and black triangles will be discussed in section 6). Since the TMI 85-GHz channel has a footprint size very close to that of the PR, no smoothing was performed.

Overall, the precipitation ice scattering increases as the reflectivity increases. In the observed relationship of S85 versus layer mean reflectivity (Fig. 10a), there are two apparent modes: one with a fast increase of scattering as the reflectivity increases, and another with a slow increase of scattering as the reflectivity increases. The fast mode is bounded with reflectivity values <30 dBZ, while the slow mode extends to higher reflectivities. Both modes are limited by S85 ≤ ~80. Recall from the earlier analysis of the ice-layer mean reflectivities in the PR observations (Figs. 2a,b) that the WCFR has typical reflectivities <30 dBZ and the NCFR is generally associated with higher reflectivity values. The two modes may correspond to the WCFR and NCFR, respectively. Given that the occurrence of graupel is generally less than that of snow in such wintertime frontal precipitation systems and might

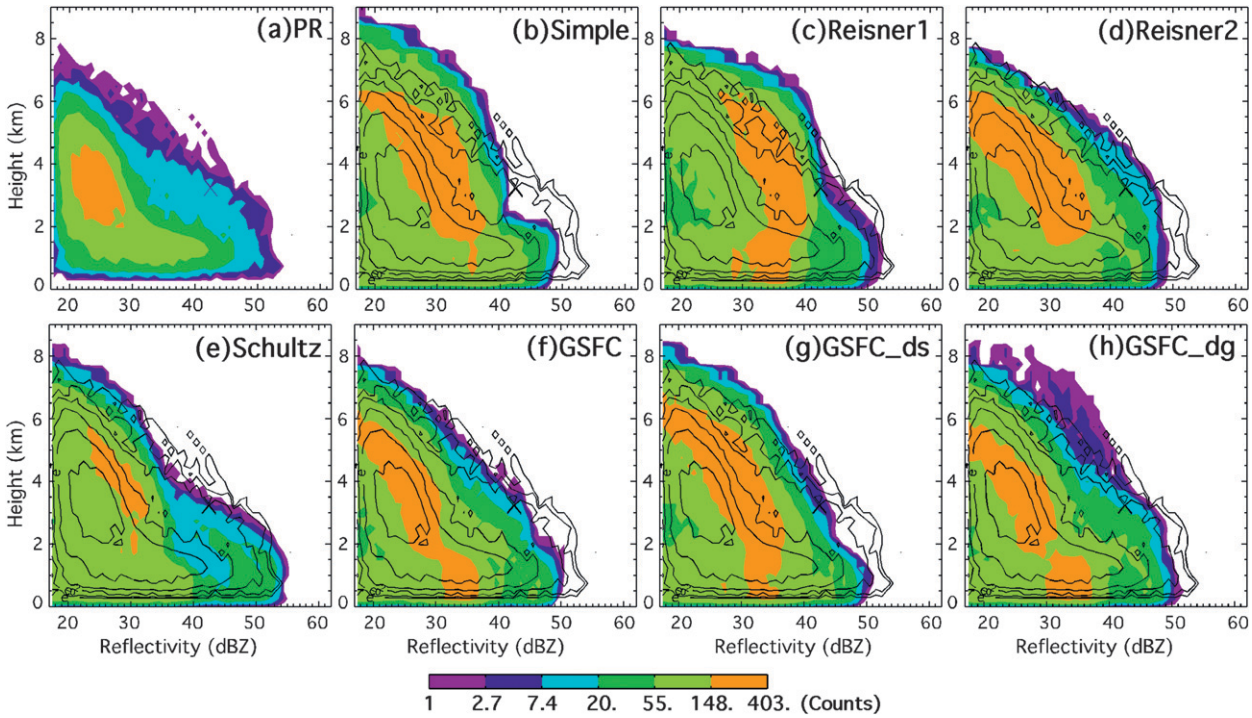

FIG. 8. Reflectivity histograms by altitude (bin size: 1 dBZ × 0.25 km) for (a) PR and (b)–(h) seven simulations. The PR observation is contoured and overlaid with the simulations.

be confined to the NCFR, the two modes shown in the 2D histogram could be related to differences in the radiative properties of the two types of precipitation ice. Evidence from the simulations will follow in sections 5d and 6.

The seven simulations appear to produce much more pronounced differences in the precipitation ice layer than in the rain layer. Consistent with the analysis of the horizontal *S85* distribution in section 4, the Simple (Fig. 10b) and GSFC (Figs. 10f–h) simulations produce maximum ice scattering that is approximately 20–30 K higher than in the observations. The Simple scheme matches the observations well at lower reflectivity (<30 dBZ), produces excessive scattering between 30 and 40 dBZ, and fails to produce reflectivities ~>40 dBZ. The GSFC and GSFC_dg runs produce higher than observed scattering at reflectivities <35 dBZ, but are better for higher reflectivities (especially GSFC_dg). The GSFC_ds run produces a generally good match to the observations except at the high end of the scattering distribution. The Reisner1 (Fig. 10c) and Schultz (Fig. 10e) runs produce maximum scattering approximately 10–20 K less than that observed. The Schultz scheme only slightly underestimate the scattering at reflectivities <30 dBZ, but significantly underestimates them at higher reflectivities. Reisner1 produces weaker than observed scattering at all reflectivities. The Reisner2 (Fig. 10d) run agrees well with the observed maximum magnitudes of the S85 value, but produces too little scattering for a given reflectivity value for values less than ~30 dBZ. In addition, the observed two modes are not apparent in most of the simulations. The Reisner1, Reisner2, Schultz runs have some ability to represent the observed slow mode, while the Simple and GSFC runs better represent the observed fast mode. With a decreased N_{0g}, the GSFC_dg run (Fig. 10h) develops a better slow mode than the other GSFC runs. In section 6, a single-layer radiative transfer model is used to better interpret the differences of the model-simulated ice properties.

d. *Partitioned role of snow and graupel on radiative transfer*

The two modes in the TRMM-observed relationship of *S85* and layer mean reflectivity suggest that the NCFR and WCFR are characterized by different microphysical and radiative properties. In addition, Han et al. (2009) found that the strength of the upward motion associated with the NCFR and WCFR differed by about one order of magnitude because of their different sources of dynamical forcing. In fact, the large contrast in upward motion between the NCFR and WCFR could favor growth of different types of precipitation ice. The analysis in the previous subsection also suggests a possible relationship

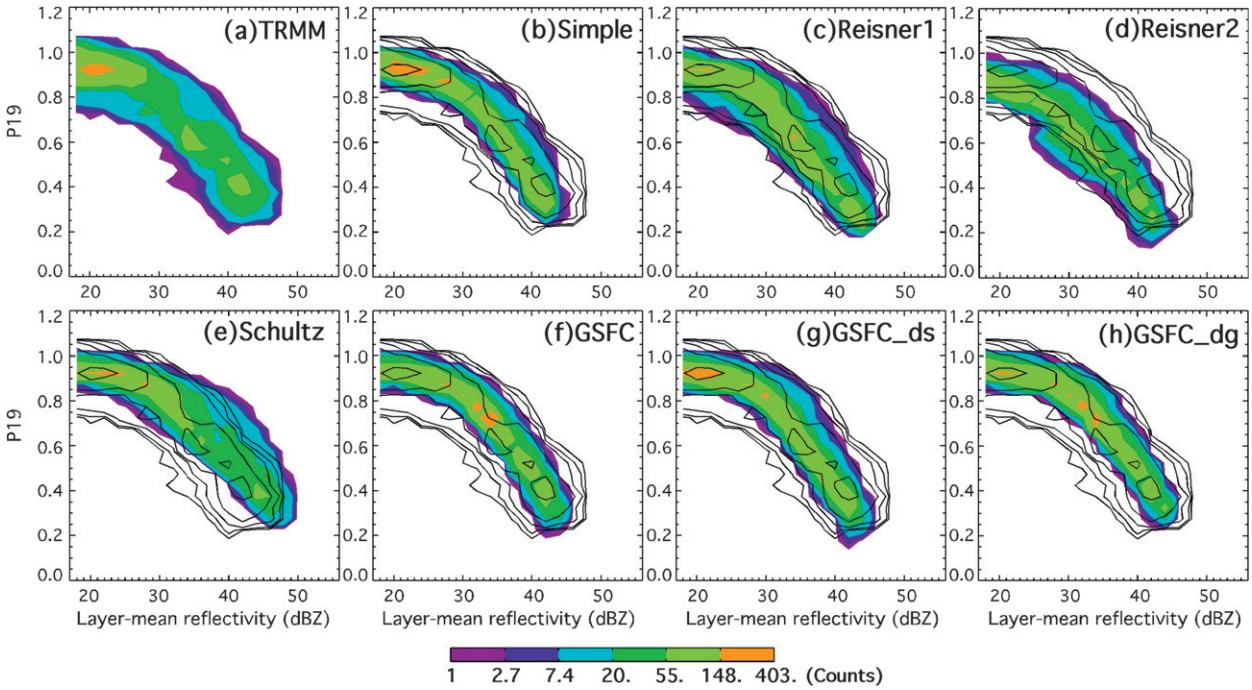

FIG. 9. The 2D histogram for rain-layer mean reflectivity (dBZ) and attenuation index P19 (bin size: 2 dBZ × 0.05 P19 unit) for (a) TRMM and (b)–(h) seven simulations. The observation is contoured and overlaid with the simulations.

between the two modes and the partitioning of snow and graupel. Therefore, the separate impacts of snow and graupel on the radiative transfer are tested in the context of the GSFC_dg simulation. The specific contribution from either snow or graupel is eliminated using two additional radiative transfer calculations, while the contributions from other hydrometeors and water vapor are retained as in the original simulation.

Before discussing the separate contributions of snow and graupel, the vertically integrated snow and graupel are shown in Figs. 11a,b, respectively, for the GSFC_dg simulation. The large amount of snow in this run is consistent with its vertical profile, shown previously. The snow is associated with both the WCFR and NCFR. The amount of graupel is limited and is largely concentrated within the NCFR (Fig. 11b).

When graupel is excluded from the radiative transfer calculation, the relationship between S85 and layer mean reflectivity due to snow can be isolated, as shown in Fig. 11c. The reflectivity associated with snow is less than 33 dBZ. The scattering increases rapidly as the reflectivity increases, in good agreement with the fast mode shown in the TRMM observations (see contours). The maximum scattering appears to be too strong, 20 K higher than the observed maximum scattering index. Figure 11d shows the contribution from graupel when snow is eliminated from the radiative transfer calculation. Graupel is associated with reflectivities up to 45 dBZ. The relationship between S85 and reflectivity for graupel is consistent with the slow mode from the TRMM observations (see contours). The GSFC_dg results suggest that, in the TRMM observations (Fig. 10a), the fast mode is associated mainly with snow in the WCFR (but also in the NCFR), while the slow mode is dominated by graupel in the NCFR.

6. A single-layer model for precipitation ice

a. Basics of a single-layer model

To interpret the differences shown in the relationship between S85 and layer mean reflectivity for precipitation ice among the various microphysical schemes, and to further investigate the contributions from snow and graupel, a single-layer model is used to solve the radiative transfer equation using Eddington's Second Approximation (Kummerow 1993). This simple model calculates the upwelling brightness temperature at the top of a single layer of precipitation ice (snow or graupel of depth H) at the TMI incident angle of 52.8° (Fig. 12a). The single layer of ice is bounded below by an opaque rain layer, assumed to emit as a blackbody at a temperature of 273 K, and above by emission from the cosmic background. Snow or graupel is homogeneously distributed in the layer. Gaseous absorption is also included. The atmospheric temperature has a constant lapse rate. It is assumed that the snow layer is 4 km deep and the graupel

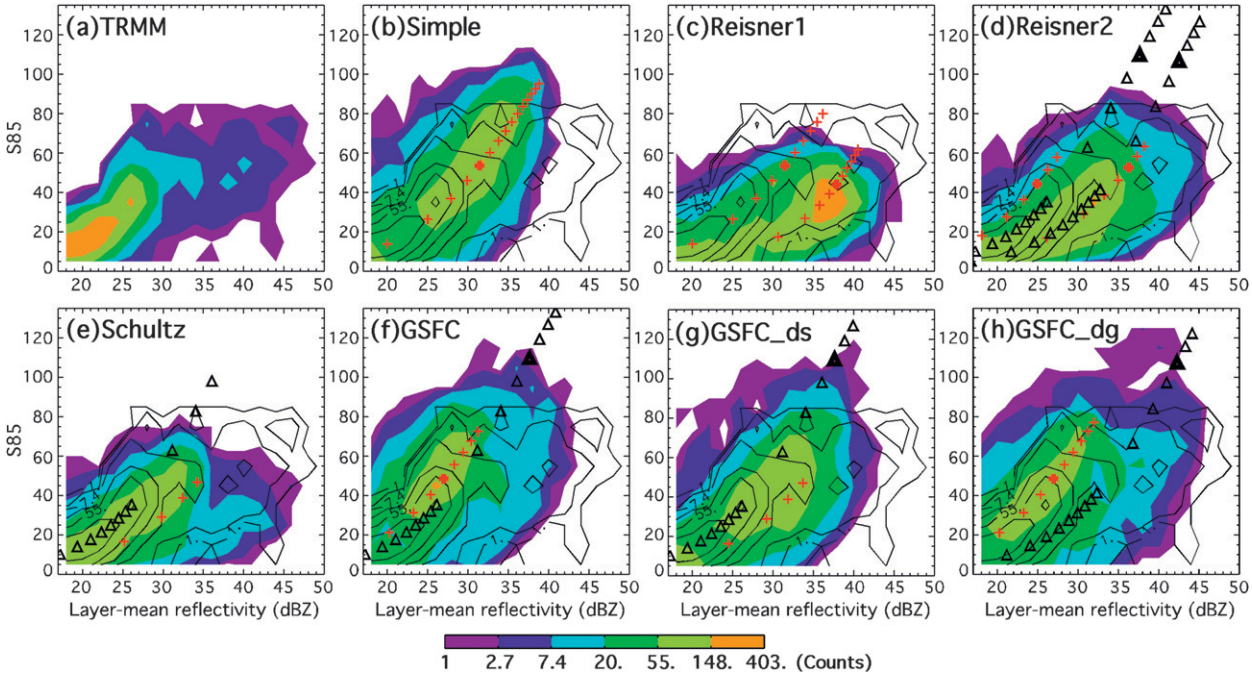

FIG. 10. As in Fig. 9, but for precipitation ice and scattering index, S85, (bin size: 2 dBZ × 10 K). The lines of crosses (red) and triangles (black) are discussed in section 6. They are taken from Fig. 12b (results from a single-layer model) with the correspondent N_{0s} and N_{0g} values for each simulation. See Table 2 for the range of water contents for each line resulted from the single-layer model calculation.

layer is 3 km deep.[7] The derived S85 parameter and the reflectivity from the single-layer model are plotted in Fig. 12b. Each curve in this plot corresponds to a specific value of N_{0s} or N_{0g} and each point in a line represents a different water content value.

For both snow and graupel, the reflectivity and scattering increase as their water contents increase. For snow, the lines (crosses) change from left to right in four clustered groups, each of which corresponds to one order of magnitude in N_{0s} as it decreases from 10^8 to 10^5 m^{-4}. For graupel, there are two groups of lines (triangles) that correspond to decreasing values of N_{0g} from 10^6 to 10^5 m^{-4}. For a given *S85* value, a smaller N_{0s} or N_{0g} results in a higher reflectivity since a decrease in N_0 leads to an increase in the mean hydrometeor size for the same water content. The reflectivity therefore increases markedly as N_0 decreases one order of magnitude. On the other hand, scattering is mainly related to the total mass of hydrometeors in a column. For a given line (a fixed N_0 value), as the snow or graupel water content increases, the total mass increases and leads to a continuous increase in the S85 value. However, for a fixed water content value (e.g., 1 g m^{-3}, see the thick crosses and triangles in Fig. 12b), when the N_0 value decreases, it shows that the scattering index either increases or decreases slightly, in contrast to the pronounced increase of the reflectivity values.

In the next subsection, lines with corresponding N_{0s} and N_{0g} values from the single-layer model calculation will be overlaid on the previous full radiative transfer calculations for each MM5 simulation. These simplified model calculations will elucidate the role of snow versus graupel and the importance of the N_{0s} and N_{0g} values in determining the differences in the relationship of scattering versus reflectivity among all the simulations as described in sections 5c and 5d.

b. Explanation for scattering versus reflectivity in the seven full model calculations

The results from the single-layer model calculations (Fig. 12b) are now overlaid on the 2D histograms of *S85* versus layer mean reflectivity from the full radiative model calculations for the seven simulations (Figs. 10b–h) to help explain the differences among the microphysical schemes. Because the water content for snow or graupel varies in each simulation, some points (crosses or triangles) are truncated from or added to the lines plotted in Fig. 12b to reflect the maximum value of the actual

[7] These layer depths are assumed based upon the ratios of total snow (or graupel) water path to layer mean snow (or graupel) water content from the full MM5 simulations.

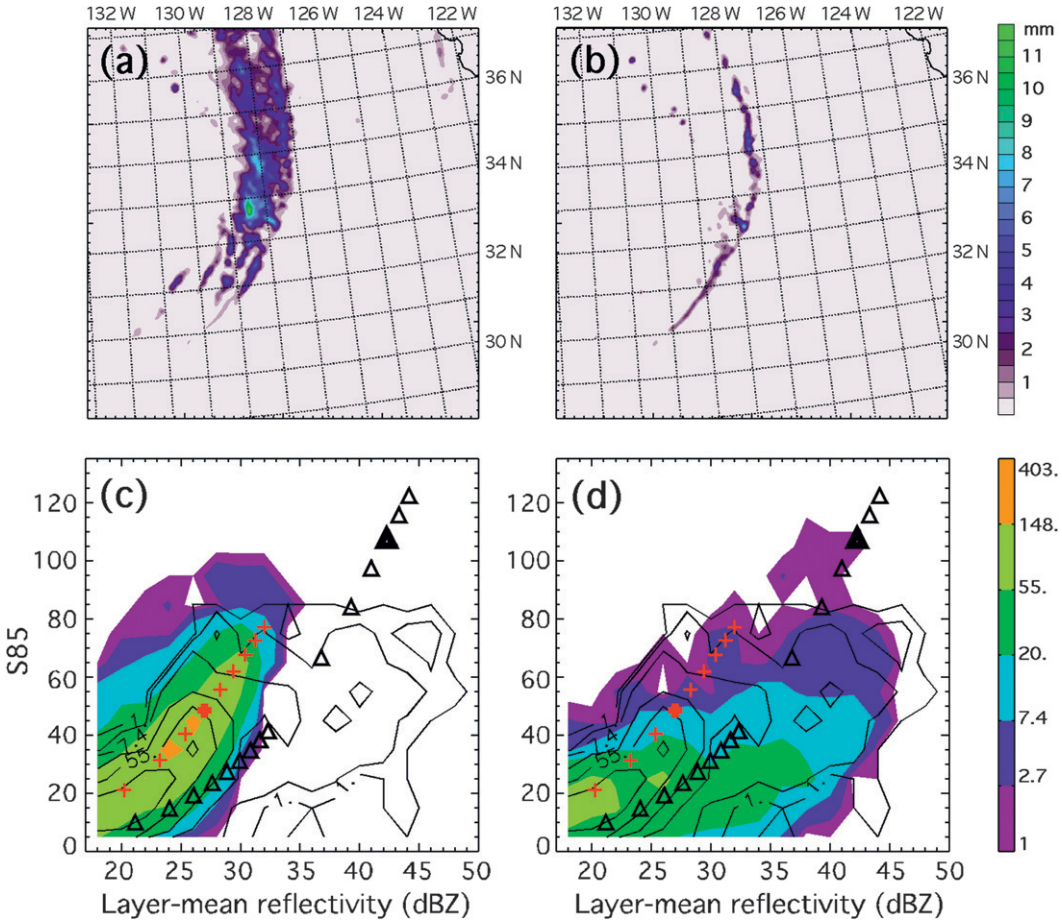

FIG. 11. Vertical-integrated (a) snow and (b) graupel for the GSFC_dg run. (c),(d) As in Fig. 10h, but for that the graupel contribution is excluded in (c) and the snow contribution is excluded in (d). The lines of crosses (red) and triangles (black) are the same as in Fig. 10h, and will be discussed in section 6.

layer mean water content for each simulation (see Table 2 for details about the magnitude of the water content). Moreover, since the contributions from snow or graupel are not explicitly calculated using the full radiative transfer model for every simulation (except the GSFC_dg run), overlaying the single-layer model results on the full radiative model calculations also provides important information for describing the partitioned radiative roles of snow and graupel for all the simulations. Generally, the single-layer model results agree well with the trend shown in the full model for each scheme. Detailed comparisons are provided below for each simulation.

In the Simple ice scheme, snow ($N_{0s} = 2 \times 10^7$ m^{-4}) is the only frozen precipitation species. Consistent with the large amount of snow shown in the hydrometeor profile, the maximum layer mean snow water content for this simulation is particularly high (~3.0 g m^{-3}). It is clear that the single-layer calculation for snow with the corresponding intercept value agrees well with the trend from the full radiative transfer calculations. In addition, the very strong scattering signatures from this simulation (~30 K higher than TMI observations) can generally be attributed to the large values of snow water content produced by this simulation.

In the Reisner1 scheme, snow is also the only category of frozen precipitation particles. This scheme defines N_{0s} as a function of snow mixing ratio and is restricted by upper (2×10^7 m^{-4}) and lower (1.2×10^5 m^{-4}) bounds (see Table 1). Both bounds are incorporated into the single-layer model calculation and overlaid on the 2D histogram of S85 versus reflectivity. Figure 10c shows that the line based on the single-layer model calculation using the lower bound N_{0s} value falls through the highest frequency in the 2D histogram; that is, this value of N_{0s} leads to good agreement with the majority of the S85–reflectivity pairs. However, the line associated with the upper bound N_{0s} corresponds to fewer points identified at the edge of the 2D histogram. Indeed, Eq. (3) shows that the typical N_{0s} for a given grid point is close to its lower bound when an appreciable amount of snow (e.g., snow mixing ratio

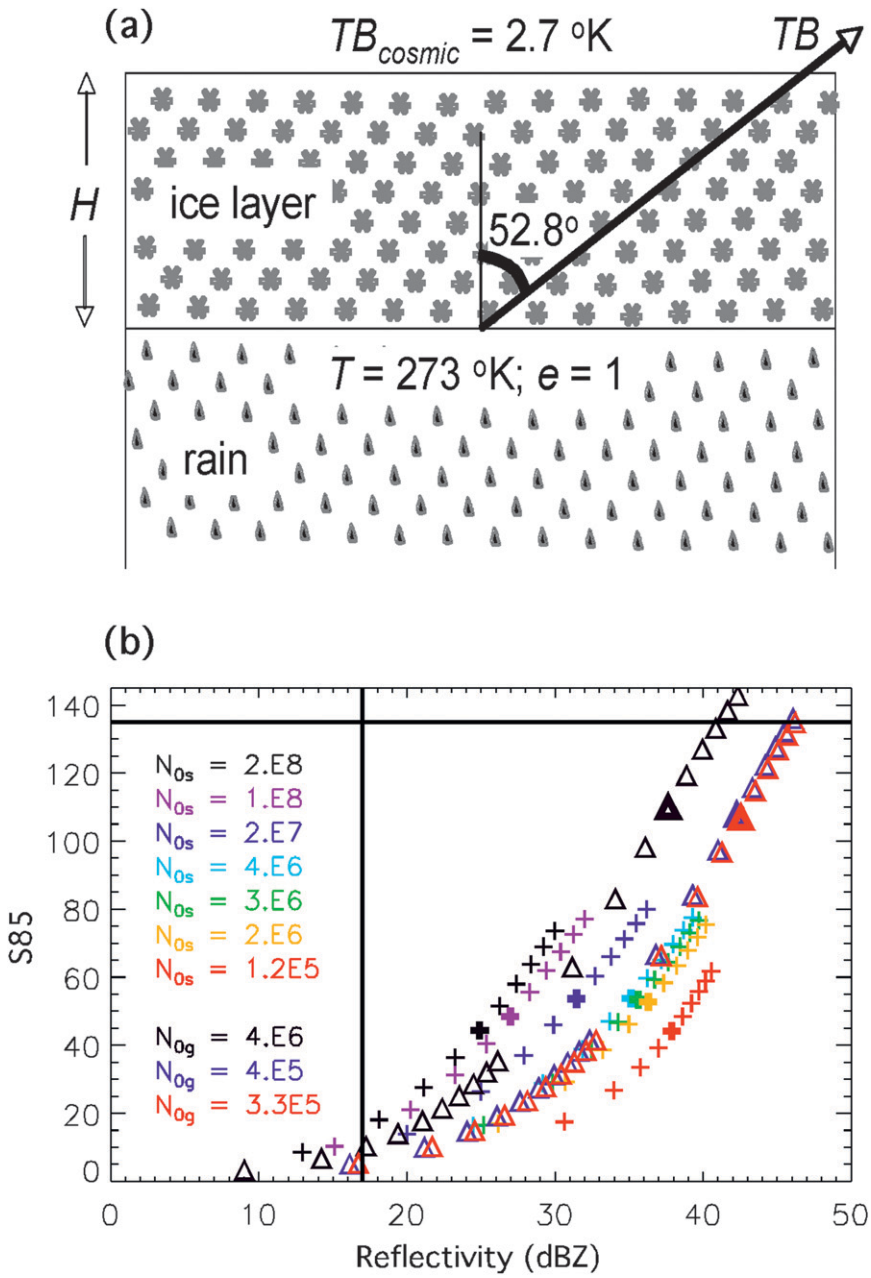

FIG. 12. (a) Schematic of a single-layer radiative transfer model. The single layer of ice (snow or graupel of depth H) is bounded below by an opaque rain layer, and above by the cosmic background. The TMI incident angle is 52.8°. (b) Relationship of scattering index S85 and reflectivity from the single-layer model with a snow layer of $H = 4$ km or a graupel layer of $H = 3$ km. Each line of crosses (triangles) is corresponding to a certain N_{0s} (N_{0g}) value with the same color shown in the legend. Each S85–reflectivity pair is corresponding to a certain water content value. The snow water content changes from 0.2 to 2 g m^{-3} with an interval of 0.2 g m^{-3}. The graupel water content changes from 0.02 to 0.2 g m^{-3} with an interval of 0.02 g m^{-3}, and then from 0.2 to 2 g m^{-3} with an interval of 0.2 g m^{-3}. The thick crosses or triangles are for snow or graupel water content of 1 g m^{-3}.

TABLE 2. Ranges of the snow and graupel water contents shown in the results of the single-layer model calculations in Fig. 10 for seven simulations.

Simulations		Simple	Reisner1	Reisner2		Schultz	GSFC	GSFC_ds	GSFC_dg
Water contents ($g\ m^{-3}$)	Snow	0.2–3.0	For upper and lower bounds 0.2–2.0	For upper bound	0.4–1.4	0.2–0.8	0.4–1.8	0.2–0.8	0.4–2.0
				For lower bound	0.2–1.4				
	Graupel	—	—	For upper bound	0.06–1.6	0.06–0.8	0.06–1.6	0.06–1.4	0.04–1.4
				For lower bound	0.04–1.6				

$>1.0\ g\ kg^{-1}$) is present. The lower bound of the intercept is therefore more representative for the variable intercept parameter for the Reisner1 run. The small N_{0s} contributes to large snow particle sizes and produces very large reflectivity values in this scheme. When considering the magnitude of the scattering, the single-layer model results show very good agreement with the full model calculations, both of which are weaker than the observed scattering.

For the Reisner2 scheme, N_{0s} is a function of the air temperature [see Eq. (4)] and N_{0g} is a function of the graupel-mixing ratio [see Eq. (5)]. Both species have upper ($N_{0s} = 2 \times 10^8\ m^{-4}$, $N_{0g} = 4 \times 10^6\ m^{-4}$) and lower ($N_{0s} = 2 \times 10^6\ m^{-4}$, $N_{0g} = 3.3 \times 10^5\ m^{-4}$) bounds. Similar to Reisner1, the lines based on the single-layer calculations corresponding to the lower bounds of N_{0s} and N_{0g} show good agreement with the majority of the data points in the 2D histogram, while the lines associated with the upper bounds lie outside the highest frequency area. The lower bounds of N_{0s} and N_{0g} are more representative of the actual N_{0s} and N_{0g} values produced in this simulation. Furthermore, in the single-layer model calculations, the lines for snow and graupel almost overlap with each other, which provides an explanation for why there is only one mode in the full model calculations. However, the more representative lower bound values may be too small and may produce excessive reflectivities that result in an agreement with the observed slow mode. The scattering produced by the single-layer model is much stronger than the full model calculation. This may be a consequence of the fact that the absorption–emission from the large amount of supercooled cloud water in the Reisner2 run is not represented by the single-layer model calculation, and this could eliminate some of the scattering due to graupel. However, further study will be needed if a detailed quantitative comparison between the full model and the single-layer model calculations is to be made.

Although the Schultz scheme does not explicitly specify the particle size distribution, the assumed N_0 values for the full radiative transfer calculation are also tested in the single-layer model (Fig. 10e). This figure shows that snow may make quite a large contribution to the reflectivity, since the assumed N_{0s} value is relatively small ($3 \times 10^6\ m^{-4}$). Considering the sensitivity of N_{0s} discussed earlier (Fig. 12b), one can argue that the Schultz scheme could yield better agreement with the TRMM observations if the conversion rates in the scheme were made to be consistent with an assumed N_{0s} value that is greater by an order of magnitude or more.

The GSFC scheme uses fixed intercept values for snow and graupel. The control run, GSFC (Fig. 10f), is conducted with the default values; that is, $N_{0s} = 1 \times 10^8\ m^{-4}$ and $N_{0g} = 4 \times 10^6\ m^{-4}$. The N_{0s} value is close to (of the same order of magnitude as) the upper bound of N_{0s} in Reisner2 scheme, while the N_{0g} value is the same as the upper bound for graupel used in the Reisner2. However, they are about one (for graupel) or two (for snow) orders of magnitude higher than the lower bounds intercepts values in Reisner2. Figure 10f shows that the lines from the single-layer model calculation for snow and graupel are very close to one another. They both cut through the high-frequency area in the 2D histogram. Similar to the Reisner2 run, the near overlapping of the snow and graupel lines is consistent with the single mode in the full model 2D histogram. However, because of the larger values of N_{0s} and N_{0g} in the GSFC run relative to the N_{0s} and N_{0g} lower bounds (the more "representative" intercept values) in Reisner2, the reflectivities in the GSFC run and its single-layer calculation are much weaker than those in the Reisner2 run for a given S85 value. Therefore, the GSFC 2D histogram appears to be in better agreement with the observed fast mode.

In the GSFC_ds sensitivity test (Fig. 10g), $N_{0s} = 4 \times 10^6\ m^{-4}$, or about two orders of magnitude less than the value in the control GSFC run. Comparing the single-layer model calculation in the GSFC_ds run (Fig. 10g) with the control GSFC run (Fig. 10f), one can find that the snow reflectivity dramatically increases ($\sim$10 dBZ) for a given snow water content. This change contributes to a shift in the full model 2D histogram from the GSFC run to the GSFC_ds run, as the former agrees better with the observed fast mode while the latter shifts toward the slow mode. However, because this shift is caused by a large increase in the reflectivity (mainly because of the decrease of N_{0s}, or increase of snow particle size), it is not consistent with the relatively small reflectivity values of snow indicated by the observations and the previous snow versus graupel partitioning analysis (see Fig. 11c).

Figure 10h shows the GSFC sensitivity run with the decreased graupel intercept parameter (GSFC_dg, $N_{0g} = 4 \times 10^5$ m^{-4}), which is one order of magnitude less than that in the GSFC control run. With a decrease in N_{0g}, the graupel reflectivity produced by the single-layer model shows a large increase, while the scattering by graupel does not change significantly as compared with the GSFC control run (see Figs. 10f and 12b). As already illustrated in the earlier snow and graupel partitioning analysis (Figs. 11c,d), the graupel line coincides with the slow mode in this run and as seen in the TRMM observations, and the snow line is in good agreement with the fast mode.

Overall, the single-layer model calculation provides a good approximation to the characteristics of the relationships of scattering versus reflectivity in the precipitation ice layer among the seven simulations using the mesoscale and the radiative transfer models. It suggests that the intercept parameters in the exponential snow and graupel size distributions have a determinative role in calculating the radiative properties of these hydrometeors, especially reflectivity. Among the seven simulations, the GSFC_dg run yields the best agreement with the TRMM observed fast and slow modes that appear to correspond to the radiative effects of snow and graupel, respectively. These calculations suggest that an N_{0s} value on the order of 10^8 m^{-4} produces the best agreement with the TRMM-observed fast mode (mainly in the WCFR region). An N_{0g} on the order of 10^5 m^{-4} produces consistency with the TRMM-observed slow mode (mainly in the NCFR region). This result indicates that the graupel in such precipitation systems may have sizes larger than those represented in the default GSFC schemes. Though the Reisner2 run yields a fairly good agreement with the observed slow mode, its small N_{0s} value might have prevented the observed fast mode from developing.

7. Conclusions

Seven simulations were conducted to quantify model biases and to evaluate the microphysics schemes available in the MM5 V3.7.4 for a winter storm using both active (PR) and passive (TMI) microwave measurements obtained by the TRMM satellite. The mesoscale model output was incorporated into a radiative transfer model to simulate the reflectivity and upwelling brightness temperatures at the PR and TMI frequencies. An attenuation index (P19) at the TMI low-frequency channel (19 GHz) and a scattering index (S85) at the high-frequency channel (85 GHz) were applied to depict the column-integrated attenuation (mainly by the rain layer) and the scattering (mainly by the precipitation ice layer), respectively. Compatible with the column-integrated nature of P19 and S85, the layer mean reflectivities within the rain or ice layer were examined. It should be noted that, because of the absence of the melting process in the radiative transfer calculations in the simulated rain layer, small errors might have been introduced to the simulated values of P19 and the rain-layer mean reflectivity. However, analysis in this paper has been restricted to the degree that the simulations should be sufficiently applicable for the focus on intrinsic features of these microphysics schemes.

The PR and TMI observations identify the characteristics of two types of frontal rainbands, the NCFR and WCFR, within the winter storm. The NCFR has much stronger reflectivity than that of the WCFR and also is associated with the strongest ice scattering. As expected, the attenuation increases as the rain-layer mean reflectivity (rain intensity) increases. The precipitation ice scattering (S85) generally increases with increasing layer mean reflectivity. However, the TMI and PR observations show what we call fast and slow modes (fast and slow increases in scattering with increasing reflectivity) in plots of scattering versus reflectivity.

Radiative transfer calculations (for the GSFC_dg run) partition the individual contributions from snow and graupel and demonstrate that, in this simulation, the fast mode consists mainly of snow that is primarily collocated with the WCFR, while the slow mode is associated with graupel in the NCFR region. Such contrasts of the major hydrometeor types in the WCFR and NCFR regions are consistent with the intensity of their updrafts in an earlier study. The partitioned radiative roles of snow and graupel are also confirmed by calculations with a single-layer radiative transfer model.

Comparisons with observations from both the PR and TMI sensors improve understanding of the performance of each scheme. In the rain layer, the results of each scheme generally agree with the observed reflectivity and attenuation to a reasonable degree. However, the Reisner2 run appears to have weaker reflectivity and stronger attenuation than the observations. The weaker reflectivity is likely due to smaller raindrop sizes, while the stronger attenuation could be caused by a greater amount of rain, both of which are attributable to the larger intercept parameter (N_{0r}) in the raindrop size distribution used in this scheme.

Although the simulations captured the general reflectivity characteristics of the frontal rainbands, the ice-layer reflectivities in the WCFR region were apparently stronger in most of the simulations than in the PR observations. The Reisner1 run has the greatest high bias (~10 dBZ). The GSFC run yields the best agreement with the observed reflectivity histogram with only a slight high bias. On the other hand, it appears more challenging for the model to replicate the scattering signatures obtained by the passive sensor (TMI). The magnitude of the

observed scattering maximum seems better represented in the Reisner2 scheme, in contrast to the excessive scattering in the Simple ice and GSFC schemes. However, there is a common problem in each simulation; that is, the strong scattering in the WCFR region disagrees with the observations and requires further investigation.

The fast and slow mode features shown in the plots of scattering versus reflectivity were not found simultaneously in most of the runs, except the GSFC_dg run to some degree. Simple radiative transfer calculations from a single-layer model readily explain the major differences between the schemes. The simple radiative transfer model shows that the reflectivities increase dramatically as the N_{0s} and N_{0g} values decrease by orders of magnitude. It also illustrates that the magnitude of the scattering is mainly attributable to the precipitation ice water contents instead of hydrometeor sizes. The different N_{0s} or N_{0g} values used in each microphysical scheme and the radiative transfer model are a determinative factor for the simulated reflectivities. At certain N_{0s} or N_{0g} values, the snow and graupel contributions overlap and cause the single-mode feature in most of the simulations. In the GSFC_dg run, the assumed N_{0s} and N_{0g} values properly differentiated the two modes (fast and slow) that are generally attributed to snow and graupel, respectively. In the Reisner1 and Reisner2 runs, their variable N_{0s} and N_{0g} formulations do not show superiority over other simulations with constant values. The most frequent N_{0s} and N_{0g} values in the Reisner runs are close to the lower bounds determined by the N_{0s} and N_{0g} formulations, which are too small and therefore produce excessively large reflectivities for a given scattering value in the two simulations.

It should be noted that, in these bulk microphysical schemes, the mean size of the precipitation hydrometeors is determined not only by the N_0 values but also by the density of each hydrometeor type, which is assumed to be fixed. Observations have found considerable variations in hydrometeor density for particles with different crystal habits, aggregation, and degree of riming, etc. (Garvert et al. 2005). This lack of hydrometeor density variation in the model could result in changes in the particle size spectrum and contributions to the some of the discrepancies between the modeled and observed radiative properties as discussed above.

Furthermore, one can assess model and observation discrepancies through investigating microphysical processes, such as autoconversion, collection, and aggregation, which control the conversion from cloud hydrometeors to precipitation. Indeed, Lang et al. (2007) reduced the collection efficiency of cloud ice and cloud water by snow and improved model simulations by reducing the snow amounts with an increase of cloud ice. In addition, Li et al. (2007) found that analyses of upper-tropospheric cloud ice in the European Centre for Medium-Range Weather Forecasts (ECMWF) model generally underestimate the amount of cloud ice compared to satellite observations. These studies suggest that the performance of the schemes in the current study may be further improved by reducing the precipitation ice growth in favor of cloud ice production, which requires future observational and modeling work. Since sensors onboard TRMM are not sensitive to cloud ice, combinations of observations from other satellites, for example, *CloudSat* and *Cloud–Aerosol Lidar and Infrared Pathfinder Satellite Observation* (*CALIPSO*), would be very beneficial in future evaluations of cloud and precipitation modeling.

The discrepancies between the model simulations and observations, as well as the large sensitivity shown in the simulated reflectivity and ice scattering signatures based on the different microphysics schemes, give some indication of the inherent uncertainty in a priori microphysical databases generated by numerical models that are used by some passive or combined passive/active precipitation retrieval algorithms. The challenge to the remote sensing and mesoscale modeling communities is to quantify these uncertainties and to evaluate the representativeness of a priori databases through rigorous comparison to well-observed atmospheric (particularly, cloud and precipitation) conditions.

Acknowledgments. The authors thank Dr. Paul Schultz at the NOAA/ESRL for his great help on understanding the Schultz scheme in the MM5. The author is very grateful for many beneficial discussions related to cloud modeling and radar with Drs. Xiaowen Li, Lin Tian, Mircea Grecu, Steve Lang, and Lihua Li at NASA/GSFC. Suggestions from Dr. Grant W. Petty at University of Wisconsin—Madison in the early stage of this study are greatly appreciated. The authors also gratefully acknowledge two anonymous reviewers and Dr. Benjamin Johnson at NASA/GSFC for their very valuable comments. This work was supported by Dr. Ramesh Kakar at NASA Headquarters with funds from the NASA Precipitation Measurement Mission science program.

REFERENCES

Anthes, R. A., and T. T. Warner, 1978: Development of hydrodynamic models suitable for air pollution and other mesometeorological studies. *Mon. Wea. Rev.,* **106,** 1045–1078.

Battan, L. J., 1973: *Radar Observation of the Atmosphere*. University of Chicago Press, 324 pp.

Braun, S. A., 2006: High-resolution simulation of Hurricane Bonnie (1998). Part II: Water budget. *J. Atmos. Sci.,* **63,** 43–64.

——, and W.-K. Tao, 2000: Sensitivity of high-resolution simulations of Hurricane Bob (1991) to planetary boundary layer parameterizations. *Mon. Wea. Rev.,* **128,** 3941–3961.

Dudhia, J., 1989: Numerical study of convection observed during the winter monsoon experiment using a mesoscale two-dimensional model. *J. Atmos. Sci.,* **46,** 3077–3107.

Fovell, R. G., and Y. Ogura, 1988: Numerical simulation of a midlatitude squall line in two dimensions. *J. Atmos. Sci.,* **45,** 3846–3879.

Garvert, M. F., C. P. Woods, B. A. Colle, C. F. Mass, P. V. Hobbs, M. T. Stoelinga, and J. B. Wolfe, 2005: The 13–14 December 2001 IMPROVE-2 event. Part II: Comparison of MM5 model simulations of clouds and precipitation with observations. *J. Atmos. Sci.,* **62,** 3520–3534.

Gilmore, M. S., J. M. Straka, and E. N. Rasmussen, 2004: Precipitation uncertainty due to variations in precipitation particle parameters within a simple microphysics scheme. *Mon. Wea. Rev.,* **132,** 2610–2627.

Han, M., S. A. Braun, P. O. G. Persson, and J.-W. Bao, 2009: Along-front variability of precipitation associated with a midlatitude frontal zone: TRMM observation and MM5 simulation. *Mon. Wea. Rev.,* **137,** 1008–1028.

Kessler, E., 1969: *On the Distribution and Continuity of Water Substance in Atmospheric Circulations*. *Meteor. Monogr.,* No. 21, Amer. Meteor. Soc., 84 pp.

Kummerow, C., 1993: On the accuracy of the Eddington approximation for radiative transfer in the microwave frequencies. *J. Geophys. Res.,* **98,** 2757–2765.

——, and Coauthors, 2001: The evolution of the Goddard profiling algorithm (GPROF) for rainfall estimation from passive microwave sensors. *J. Appl. Meteor.,* **40,** 1801–1820.

Lang, S., W.-K. Tao, R. Cifelli, W. Olson, J. Halverson, S. Rutledge, and J. Simpson, 2007: Improving simulations of convective systems from TRMM LBA: Easterly and westerly regimes. *J. Atmos. Sci.,* **64,** 1141–1164.

Li, J.-L., J. H. Jiang, D. E. Waliser, and A. M. Tompkins, 2007: Assessing consistency between EOS MSL and ECMWF analyzed and forecast estimates of cloud ice. *Geophys. Res. Lett.,* **34,** L08701, doi:10.1029/2006GL029022.

Li, X., W.-K. Tao, T. Matsui, C. Liu, and H. Masunaga, 2009: Improving a spectral bin microphysical scheme using TRMM satellite observations. *Quart. J. Roy. Meteor. Soc.,* **136,** 382–399.

Lin, Y.-L., R. D. Farley, and H. D. Orville, 1983: Bulk parameterization of the snow field in a cloud model. *J. Climate Appl. Meteor.,* **22,** 1065–1092.

Liu, C., and M. W. Moncrieff, 2007: Sensitivity of cloud-resolving simulations of warm-season convection to cloud microphysics parameterizations. *Mon. Wea. Rev.,* **135,** 2854–2868.

Marshall, J. S., and W. M. Palmer, 1948: The distribution of raindrops with size. *J. Atmos. Sci.,* **5,** 165–166.

Matsui, T., X. Zeng, W.-K. Tao, H. Masunaga, W. S. Olson, and S. Lang, 2009: Evaluation of long-term cloud-resolving model simulations using satellite radiance observations and multifrequency satellite simulators. *J. Atmos. Oceanic Technol.,* **26,** 1261–1274.

McCumber, M., W.-K. Tao, J. Simpson, R. Penc, and S.-T. Soong, 1991: Comparison of ice-phase microphysical parameterization schemes using numerical simulations of tropical convection. *J. Appl. Meteor.,* **30,** 985–1004.

McFarquhar, G. M., H. Zhang, G. Heymsfield, R. Hood, J. Dudhia, J. B. Halverson, and F. Marks Jr., 2006: Factors affecting the evolution of Hurricane Erin (2001) and the distribution of hydrometeors: Role of microphysical processes. *J. Atmos. Sci.,* **63,** 127–150.

Mugnai, A., E. A. Smith, G. J. Tripoli, S. Dietrich, V. Kotroni, K. Lagouvardos, and C. M. Medaglia, 2008: Explaining discrepancies in passive microwave cloud-radiation databases in microphysical context from two different cloud-resolving models. *Meteor. Atmos. Phys.,* **101,** 127–145.

Olson, W. S., P. Bauer, N. F. Viltard, D. E. Johnson, W.-K. Tao, R. Meneghini, and L. Liao, 2001a: A melting-layer model for passive/active microwave remote sensing applications. Part I: Model formulation and comparison with observations. *J. Appl. Meteor.,* **40,** 1145–1163.

——, ——, C. D. Kummerow, Y. Hong, and W.-K. Tao, 2001b: A melting-layer model for passive/active microwave remote sensing applications. Part II: Simulations of TRMM observations. *J. Appl. Meteor.,* **40,** 1164–1179.

Petty, G. W., 1994: Physical retrievals of over-ocean rain rate from multichannel microwave imagery. Part I: Theoretical characteristics of normalized polarization and scattering indices. *Meteor. Atmos. Phys.,* **54,** 79–99.

——, and K. B. Katsaros, 1990: Precipitation observed over the South China Sea by the Nimbus-7 Scanning Multichannel Microwave Radiometer during winter MONEX. *J. Appl. Meteor.,* **29,** 273–287.

Reisner, J., R. M. Rasmussen, and R. T. Bruintjes, 1998: Explicit forecasting of supercooled liquid water in winter storms using the MM5 mesoscale model. *Quart. J. Roy. Meteor. Soc.,* **124,** 1071–1107.

Rutledge, S. A., and P. V. Hobbs, 1984: The mesoscale and microscale structure and organization of clouds and precipitation in midlatitude cyclones. XII: A diagnostic modeling study of precipitation development in narrow cold frontal rainbands. *J. Atmos. Sci.,* **41,** 2949–2972.

Schultz, P., 1995: An explicit cloud physics parameterization for operational numerical weather prediction. *Mon. Wea. Rev.,* **123,** 3331–3343.

Tao, W.-K., and J. Simpson, 1993: Goddard cumulus ensemble model. Part I: Model description. *Terr. Atmos. Ocean Sci.,* **4,** 35–72.

——, ——, and M. McCumber, 1989: An ice–water saturation adjustment. *Mon. Wea. Rev.,* **117,** 231–235.

Thompson, G., R. M. Rasmussen, and K. Manning, 2004: Explicit forecasts of winter precipitation using an improved bulk microphysics scheme. Part I: Description and sensitivity analysis. *Mon. Wea. Rev.,* **132,** 519–542.

Yuter, S. E., and R. A. Houze Jr., 1995: Three-dimensional kinematic and microphysical evolution of Florida cumulonimbus. Part II: Frequency distributions of vertical velocity, reflectivity, and differential reflectivity. *Mon. Wea. Rev.,* **123,** 1941–1963.